ANNUAL REVIEWS

Annual Review of Nuclear and Particle Science

Neutrino Emission as Diagnostics of Core-Collapse Supernovae

B. Müller

Monash Centre for Astrophysics, School of Physics and Astronomy, Monash University, Clayton, Victoria 3800, Australia; email: bernhard.mueller@monash.edu

Annu. Rev. Nucl. Part. Sci. 2019. 69:253–78

First published as a Review in Advance on August 6, 2019

The *Annual Review of Nuclear and Particle Science* is online at nucl.annualreviews.org

https://doi.org/10.1146/annurev-nucl-101918-023434

Keywords

core-collapse supernovae, neutrinos, neutron stars

Abstract

With myriads of detection events from a prospective Galactic core-collapse supernova, current and future neutrino detectors will be able to sample detailed, time-dependent neutrino fluxes and spectra. This will offer significant possibilities of inferring supernova physics from the various phases of the neutrino signal, ranging from the neutronization burst through the accretion and early explosion phases to the cooling phase. The signal will constrain the time evolution of bulk parameters of the young proto–neutron star, such as its mass and radius, as well as the structure of the progenitor; probe multidimensional phenomena in the supernova core; and constrain the dynamics of the early explosion phase. Aside from further astrophysical implications, supernova neutrinos may also shed light on the properties of matter at supranuclear densities and on open problems in particle physics.

Contents

1. INTRODUCTION

The collapse and the ensuing explosion of massive stars as a core-collapse supernova constitute one of the most intriguing processes in astrophysics in which neutrinos play a crucial role in the dynamics of a macroscopic system, as well as one of the few detectable sources of neutrinos outside the Solar System.

1.1. Dynamics of Collapse and Explosion

Many elements of this phenomenon have been well established theoretically, and have even been corroborated to some degree by the groundbreaking detection of about two dozen neutrinos from SN 1987A in the Large Magellanic Cloud (1–3). The phase of collapse and bounce is now well understood and has been discussed extensively in a classic paper (4) and in other reviews (5, 6): Once the Fe core of the progenitor star grows to roughly the Chandrasekhar mass and has reached sufficiently high densities by quasi-static contraction, electron captures on heavy nuclei and photodisintegration of heavy nuclei (the latter being more important for higher core entropy) eventually lead to collapse on a dynamical timescale. As the density and the electron chemical potential increase, electron captures on heavy nuclei and the few free protons that are present in nuclear statistical equilibrium (NSE) happen more rapidly and accelerate the collapse. Initially, the electron neutrinos (ν_e) produced by the electron captures leave the core unimpeded, until the neutrino mean free path becomes comparable to the core radius at densities of $\sim 10^{11}\,\mathrm{g\,cm^{-3}}$ so that the emitted neutrinos are trapped and further loss of lepton number from the core (deleptonization) ceases. However, this does not halt the collapse, which only stops once the core density overshoots nuclear saturation density and the repulsive nuclear forces lead to a stiffening of the equation of state (EoS) and an elastic rebound (bounce) of the homologous inner core. In the wake of the

NSE: nuclear statistical equilibrium

bounce, a shock wave is launched at the edge of the inner core. The shock quickly turns into a stalled accretion shock as the initial energy of the rebound is consumed by the disintegration of heavy nuclei into free nucleons in the shock, and by rapid neutrino losses once the shock reaches densities of $\sim 10^{11}$ g cm^{-3}. The position of the shock then adjusts quasi-statically to the decreasing mass accretion rate, reaching a maximum radius of 100–200 km approximately 100 ms after bounce before slowly receding again.

How the stalled shock is then revived in most progenitors (i.e., made to propagate out dynamically to expel the outer layers of the star) remains the subject of active research (see References 7–10 for reviews). The most promising scenario for the majority of core-collapse supernovae is the delayed neutrino-driven mechanism (11). In the neutrino-driven paradigm, the shock is revived thanks to the reabsorption of a fraction of the neutrinos emitted from the proto–neutron star (PNS) surface in the gain region behind the shock. If neutrino heating is sufficiently strong, the increase in thermal pressure pushes the shock outward, which in turn increases the mass of the gain region and hence the efficiency of neutrino heating so that runaway shock expansion ensues. In all but the least massive progenitors (12), the neutrino heating needs to be supported by multidimensional fluid instabilities such as convective overturn (13–15) or the standing accretion-shock instability (SASI) (16, 17), which manifests as dipolar or quadrupolar shock oscillations. One alternative to this scenario is the magnetorotational mechanism (e.g., 18–21), which may explain the small fraction of unusually energetic hypernovae with explosion energies of up to $\sim 10^{52}$ erg, but which requires rapidly rotating progenitors. There are many indications from, for instance, the birth spin periods of pulsars (22) and asteroseismic measurements of core rotation in low-mass stars (23) that such rapidly rotating progenitors are rare, and that the cores of massive stars typically rotate slowly due to efficient angular momentum transport in stellar interiors. Other mechanisms have also been proposed, most notably the phase-transition mechanism of References 24 and 25, which involves a second collapse and bounce of the PNS after a hypothetical first-order QCD phase transition that launches another shock wave that is sufficiently powerful to explode the star.

Proto–neutron star (PNS): the hot and still relatively proton-rich compact remnant during the early seconds of a supernova that later deleptonizes and cools to become a veritable neutron star

Gain region: the region behind the shock where neutrino heating dominates over neutrino cooling

SASI: standing accretion-shock instability

1.2. Neutrino Emission: Rough Estimates and Scales

Regardless of the supernova mechanism, neutrinos dominate the energy budget of the supernova core and carry away most of the energy liberated by gravitational collapse, which is essentially equal to the binding energy $E_{\rm bind}$ of the young neutron star. $E_{\rm bind}$ is of the order of GM^2/R in terms of the (gravitational) neutron star mass M and radius R; a more precise fit to solutions of the stellar structure equations yields (26)

$$E_{\rm bind} \approx 0.6 \frac{GM^2}{R} \left(1 - \frac{1}{2}\frac{GM}{Rc^2}\right)^{-1}. \qquad 1.$$

Because of neutrino trapping, this energy is radiated away only on timescales of seconds with total luminosities of all flavors of $\sim 10^{53}$ erg s^{-1}. As the neutrinos decouple from the matter only at the neutrinosphere at the PNS surface during the first few seconds of its life, their emerging spectrum reflects an environment with a temperature of a few MeV rather than tens of MeV in the PNS interior. Together with the radius of the neutrinosphere, the PNS surface temperature sets the scale for the luminosity according to the Stefan–Boltzmann law,

$$L_\nu \sim 4\pi \sigma_{\rm fermi} R^2 T^4, \qquad 2.$$

where $\sigma_{\rm fermi} = 4.50 \times 10^{35}$ erg MeV^{-4}s^{-1}cm^{-2} is the radiation constant for massless fermions with vanishing degeneracy.

IBD: inverse β decay

On the basis of such simple considerations, the detection of neutrinos from SN 1987A (1–3) was already sufficient to validate the basic theoretical picture of core collapse. The total count, energy, and timing of the detected neutrinos established that a compact object with a binding energy of a few 10^{53} erg (assuming equipartition between flavors) was formed and emitted neutrinos for a few seconds from a surface region with a radius of tens of kilometers and a temperature of a few MeV (27–30).

The neutrino signal from a prospective Galactic supernova could provide considerably more information on the dynamics in the supernova core and in the progenitor, as well as on problems in nuclear and particle physics. With current and future instruments, the principal difference with regard to the case of SN 1987A would consist of better statistics, which would provide detailed time-dependent fluxes for the arriving electron antineutrinos ($\bar{\nu}_e$) and to a lesser extent the ν_e, allow for a much better determination of the neutrino energy spectrum, and constrain the flux of heavy-flavor neutrinos to some degree.

Some excellent reviews on the supernova neutrino signal have recently been written and may be consulted for further reference. This review seeks to fill the middle ground with less of a focus on the basic physical principles (neutrino transport, weak interaction rates, etc.) and a broader coverage of the diagnostic potential of the neutrino signal than Reference 31 but a more selective and compressed approach than the extensive reviews in References 32 and 33.

2. PREPARING FOR THE NEXT GALACTIC SUPERNOVA

2.1. Prospects for Supernova Neutrino Detection

Current and future supernova neutrino detectors employ different detector materials and detection principles and will complement one another in the event of a Galactic supernova. Water Cherenkov detectors can accommodate large detector volumes and will have the highest count rates. They are sensitive primarily to $\bar{\nu}_e$ via the inverse β decay (IBD) reaction $\bar{\nu}_e + p \rightarrow n + e^+$. Classical water Cherenkov detectors are capable of measuring the energies of detected MeV neutrinos; examples include the operational Super-Kamiokande (Super-K) detector (34), with ~10,000 events for a Galactic supernova at a typical distance of 10 kpc, and its planned successor, Hyper-Kamiokande (Hyper-K) (35), with ~250,000 events. Particularly large detector volumes can be realized in long-string water Cherenkov detectors such as IceCube (36). However, MeV neutrinos will be detected only through an increase in the dark current in such detectors, and no energy information will be available. The primary advantages of IceCube for supernova neutrino detection are its excellent time resolution and high total event count of 10^5–10^6 events.

In liquid scintillator detectors, IBD is also the primary detection channel, but since they are limited to smaller volumes, the expected count rates are lower than for Hyper-K, with ~15,000 and ~5,000 IBD events for the future JUNO (37) and LENA (38) detectors, respectively. However, they offer excellent energy resolution and allow for the reconstruction of the ν_e signal to some degree. Liquid scintillator detectors currently in operation (KamLAND, Borexino, Baksan, etc.) will detect only a few hundred events unless the supernova is exceptionally close. The NOvA detectors also have a sufficiently large volume to observe a few thousand events but are geared toward GeV neutrinos; work on supernova neutrino detection with these instruments is in progress (39).

Liquid argon detectors provide the best handle on the ν_e signal through the reaction $\nu_e + {}^{40}\mathrm{Ar} \rightarrow {}^{40}\mathrm{K} + e^-$. With a detector mass of 40 kton, the future DUNE detector (40) will provide good sampling of the ν_e light curves with ~3,000 events for a supernova at 10 kpc.

Heavy-flavor neutrinos (hereafter, ν_x) will be detected only via neutral-current scattering events, primarily neutrino–electron scattering in water Cherenkov detectors, as well as

neutrino–proton scattering in liquid scintillator detectors. Although future detectors will measure a sizable number of scattering events (e.g., a few thousand in LENA), the reconstruction of the ν_x flux is not trivial: The ν_x are conflated with ν_e and $\bar{\nu}_e$ in the scattering channel, and the exact energy of the scattered neutrino cannot be reconstructed. For more information and other detector types, see the dedicated reviews on supernova neutrino detection (32, 41).

2.2. Neutrino Signal Predictions: Theoretical Challenges and Uncertainties

There is a flip side to the prospect of accurate, time-dependent measurements of supernova neutrino fluxes and spectra: In contrast to the historic example of SN 1987A, uncertainties in the predicted neutrino emission on the level of a few percent or more can become relevant for inferring physical parameters. Such uncertainties concern various aspects of the supernova problem, such as numerical approximations for neutrino transport and neutrino–matter interaction rates. These cannot be treated at length here, so the reader is referred to the literature. The strengths and weaknesses of currently employed methods for neutrino transport are discussed in References 10 and 42, and a number of recent papers have helped to gauge uncertainties in the modeling by code comparisons (e.g., 43–49) and by investigating variations in the neutrino interaction rates (e.g., 25, 50–58).

There are also unresolved problems concerning neutrino flavor conversion in supernova cores that translate into uncertainties in the observable fluxes in the different flavors. Specifically, research on collective oscillations is still very much in a state of flux, so this review merely outlines the problem and refers the reader elsewhere (32, 59) for more detailed overviews.

Flavor conversion in supernovae is determined by the interplay of three different types of terms in the neutrino Hamiltonian. The vacuum terms and the matter terms that arise from neutrino forward scattering on charged leptons give rise to the two familiar Mikheyev–Smirnov–Wolfenstein (MSW) resonances (60, 61) at densities of $\sim 10^3\,\mathrm{g\,cm^{-3}}$ (H-resonance) and $\sim 10\,\mathrm{g\,cm^{-3}}$ (L-resonance). The effect of the MSW resonances alone is rather well understood; with the three neutrino flavors in the Standard Model, the outcome depends on the (unknown) mass hierarchy and the structure of the star in the resonance regions (adiabatic versus nonadiabatic conversion). As a rule of thumb, MSW flavor conversion in the normal mass hierarchy alone would result in a complete swap of ν_e for ν_x and a high survival rate of 0.68 for $\bar{\nu}_e$ for most progenitors during the early signal phase; for an inverse mass hierarchy, the survival rates of ν_e and $\bar{\nu}_e$ would be 0.32 and 0, respectively. Some refinements of this picture are discussed in Sections 3 and 5.2, below.

However, flavor conversion in supernovae is complicated by the high neutrino number densities in the environment of the PNS. Under these conditions, the terms for neutrino–neutrino forward scattering (i.e., neutrino self-refraction) in the Hamiltonian can no longer be ignored (e.g., 62, 63) and drive collective flavor conversion of neutrinos and antineutrinos that conserves lepton family number. The self-refraction terms turn flavor conversion into a nonlinear problem with an extremely complex phenomenology that is not yet fully understood. Additional flavor conversion modes have appeared whenever new dimensions—such as the angular distribution of neutrinos in phase space—were added to the problem (e.g., 64–68), and the numerical treatment is rife with pitfalls that give rise to spurious instabilities (69, 70). During the pre-explosion phase, the matter terms may be sufficiently large to suppress collective flavor conversion (71, 72), but the verdict on the conditions and outcome of these collective oscillations is still pending.

3. COLLAPSE AND NEUTRINO BURST

Even before the onset of collapse, a supernova progenitor is already a strong source of MeV neutrinos that come mostly from thermal emission processes during advanced burning stages. For

nearby supernovae, the neutrino emission from the core Si-burning stage may be detectable as the first signature of the impending collapse by future liquid scintillator detectors such as JUNO and DUNE, or already by Super-K if doped with gadolinium (73–77). This would not only provide an advance warning for the supernova but could also serve as a diagnostic for the progenitor mass and even reveal the timing of some of the final core- and shell-burning episodes (75). Improvements are still needed, however, to gauge the full diagnostic potential of presupernova neutrinos, for example, by a more rigorous treatment of the emission processes, including β processes (77).

When collapse of the Fe core starts in earnest, the production of ν_e by electron captures on heavy nuclei and the few free protons available in NSE becomes the dominant source of neutrinos. The ν_e luminosity increases to approximately 10^{53} erg s^{-1} around the time of trapping, and the mean energy climbs to ~10 MeV. Trapping then leads to a small dip in the luminosity as neutrino leakage is confined to a narrow region around the newly formed neutrinosphere. Neutrino emission again increases rapidly after core bounce as the newly formed shock propagates into regions of sufficiently low density and reaches the neutrinosphere. Due to shock heating and low optical depth, neutrinos are swiftly released in copious amounts from the shocked matter, mostly via electron captures on free protons. The emission of ν_e dominates by far since the electron fraction Y_e in the shocked matter is still relatively high and far above the β equilibrium value, with ν_e luminosities transiently reaching 3.5×10^{53} erg s^{-1} in what is known as the neutronization burst (see **Figure 1** for typical light curves and neutrino mean energies during the first seconds of a supernova).

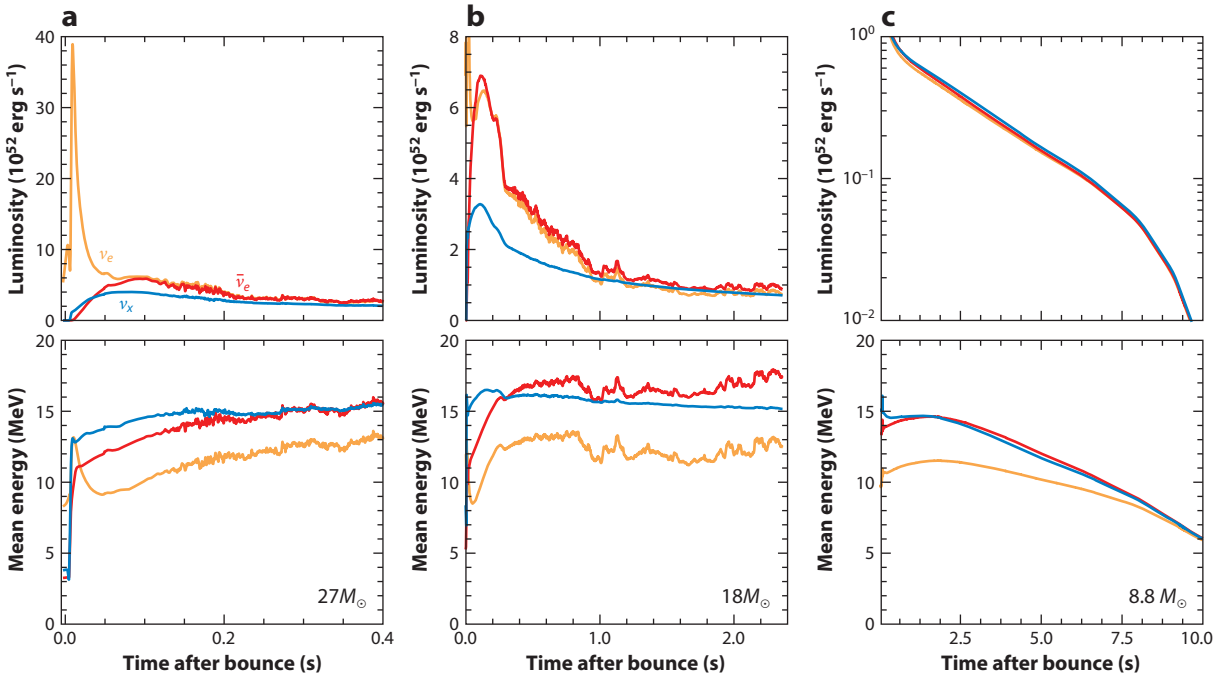

Figure 1

Neutrino luminosities and mean energies from different simulations. (*a*) The two-dimensional model of a $27M_\odot$ star (78) illustrates the burst phase, the accretion phase, and the early explosion phase with the characteristic excess in the luminosity of ν_e and $\bar{\nu}_e$. (*b*) The three-dimensional explosion model of an $18M_\odot$ star (79) extends further into the explosion phase and shows the luminosities of different flavors moving closer to equipartition as accretion subsides. (*c*) The $8.8M_\odot$ electron-capture supernova model (45) shows the Kelvin–Helmholtz cooling phase with good equipartition and a visible decline of neutrino mean energies after ~1.5 s.

The burst has substantial diagnostic value since its shape is quite robust with little dependence on the progenitor mass or the nuclear EoS (80): With a megaton water Cherenkov detector such as Hyper-K, the burst could be used as a standard candle for a distance determination within ∼5%. Moreover, the observation or nonobservation of the ν_e burst constrains the mass hierarchy, which determines the ν_e survival probability in the MSW resonance regions. In the normal mass hierarchy, the burst neutrinos would leave the star in the third mass eigenstate and thus hit detectors on Earth with only a tiny overlap with the ν_e flavor eigenstate.

ZAMS: zero-age main sequence

Another independent handle on the mass hierarchy could come from the signal of $\bar{\nu}_e$ and ν_x (81). Although ν_e emission dominates during the burst, the light curves of ν_x begin to rise during the burst as thermal emission processes (electron–positron pair annihilation, bremsstrahlung, and neutrino pair conversion) become important in the shock-heated matter. The emission of $\bar{\nu}_e$ by charged-current processes is inhibited as long as the matter is still more proton-rich than in β equilibrium, so that the $\bar{\nu}_e$ light curve rises more slowly than that of ν_x. Since the mass hierarchy determines how the emission of $\bar{\nu}_e$ and $\bar{\nu}_x$ in the supernova core translates into $\bar{\nu}_e$ and $\bar{\nu}_x$ after the neutrinos undergo MSW flavor conversion at radii of tens of thousands of kilometers, the fast or slow rise of the detected $\bar{\nu}_e$ signal on Earth would point to an inverted or normal mass hierarchy, respectively (81).

For a special core-collapse supernova channel arising from super-asymptotic giant branch (SAGB) stars (see the sidebar titled Electron-Capture Supernovae), flavor conversion during this early phase of neutrino emission works in a distinctly different manner, which implies that a neutrino detection could provide a smoking gun for such SAGB progenitors. These progenitors are low-mass stars with a zero-age main sequence (ZAMS) mass of around $8M_\odot$ (for single stars), which do not go through all the hydrostatic burning stages up to the formation of an Fe core but rather undergo collapse due to electron captures on ^{20}Ne and ^{24}Mg in a highly degenerate O–Ne–Mg core (82–84), and then explode as electron-capture supernovae with low explosion energies (12). They exhibit a very steep density gradient outside the degenerate core, which moves the MSW resonances relatively close together, makes the MSW flavor conversion nonadiabatic, and assigns a larger role to nonlinear collective neutrino interactions because of the low electron number densities. The emerging neutrino spectra exhibit a spectral swap at 11–15 MeV (depending on the mass hierarchy) with a survival probability of ∼0.68 for ν_e of higher energies as these neutrinos jump to the first mass eigenstate (85). If such a high survival probability is measured for the burst neutrinos (which presupposes that the distance to the supernova can be inferred by

ELECTRON-CAPTURE SUPERNOVAE

The collapse of a star with an O–Ne–Mg core due to electron capture is a channel toward core collapse that is still poorly understood. Whether a star that has undergone carbon core burning and evolves into an SAGB star can eventually collapse and explode as an electron-capture supernova (ECSN) hinges on many uncertainties regarding mass loss, mixing processes, and turbulent flame propagation and nuclear physics after off-center O ignition (84, 87–89). This progenitor channel is likely very narrow for single stars of solar metallicity (88, 90) but may be wider at lower metallicity and in interacting binaries (90). To date, no observed transient has been unambiguously identified as an ECSN, although various candidates have been proposed, including the historic Crab supernova (91, 92), SN 2008S (93), SN 2005cs (94), and the subclass of type IIn-P supernovae (92) with narrow (n) emission lines. Even for a Galactic ECSN, uncertainties in the envelope structure and the presence of circumstellar material may complicate the interpretation of the electromagnetic transient, and a smoking gun for an SAGB progenitor from the neutrino signal would be most valuable.

other means), this would furnish direct proof of an SAGB progenitor. The later phases of the signal could bolster such a progenitor determination further, as has been shown (86) for the case of the normal mass hierarchy: As the shock hits the MSW resonances and the density gradients become shallower, the MSW conversion becomes more adiabatic so that the ν_e survival probability essentially drops to zero about 100 ms after bounce.

The ν_e burst and the rise phase of the $\bar{\nu}_e$ and ν_x signal also allow for precise timing of the bounce. The survival of the ν_e burst after oscillations is not critical for this; assuming normal mass ordering (so that the ν_e burst would not be observed in liquid argon detectors), IceCube will still be able to pinpoint the bounce to approximately 3.5 ms by using the rise of the measured $\bar{\nu}_e$ flux (95). The timing of the bounce is also relevant in the context of concurrent neutrino and gravitational wave detections. The neutrino signal is useful for gravitational wave detection as it helps define the period of interest for a signal search in a noisy data stream (96). If there are correlated features in the neutrino and gravitational wave signals, they can be exploited to improve parameter estimation, and the bounce of rotating progenitors provides the prime example. In this case, there will be a strong gravitational wave signal from the bounce of the rotationally deformed core (e.g., 97), which is roughly coincident with the neutrino burst. This temporal correlation can be used to more accurately determine the time of bounce and the degree of rotation (96). For sufficiently rapid rotation, the early neutrino signal also shows temporal modulations, whose frequency is set by the fundamental quadrupole mode that dominates the gravitational wave spectrum (98). However, even with Hyper-K and for the most rapidly spinning PNSs, these modulations in the neutrino signal will be detectable only to ∼1 kpc (98).

4. THE SIGNAL FROM THE ACCRETION AND EARLY EXPLOSION PHASES

Over timescales of tens of milliseconds, the supernova core develops a characteristic structure during the pre-explosion phase (**Figure 2**): The accretion shock sits at a radius of 100–200 km, and below it there is an extended hot-bubble region of high entropy. The EoS in this region is dominated by photons and electron–positron pairs, and heating by neutrinos from further inside dominates over neutrino cooling. At moderately high densities of $\sim 10^{10}\,\mathrm{g\,cm^{-3}}$ to $10^{13}\,\mathrm{g\,cm^{-3}}$ further inside, the pressure is provided mostly by baryons and is roughly described by an ideal gas law, $P \propto \rho T$. Close to the transition between these two EoS regimes, neutrino cooling starts to dominate over heating. Further within the core of the PNS, the EoS is dominated by nuclear interactions. Because of shock heating in the layers outside the small inner core of $\sim 0.5 M_\odot$ (99) that remained in homologous collapse until bounce, the maximum temperature is reached off-center in an extended mantle of moderate entropy between the core and the surface.

4.1. Constraining Parameters of the Proto–Neutron Star and the Accretion Flow

The emission of electron-flavor and heavy-flavor neutrinos is distinctly different in this environment. For all flavors, there is a diffusive flux to the PNS surface region driven by gradients in temperature and neutrino chemical potential. This diffusive flux is essentially determined by the temperature and radius of the decoupling region (neutrinosphere) near the PNS surface, that is, by bulk parameters of the PNS. This component of the neutrino flux can be well described by the gray-body emission law

$$L_{\mathrm{diff}} = 4\pi\phi\sigma_{\mathrm{fermi}} R^2 T^4, \qquad 3.$$

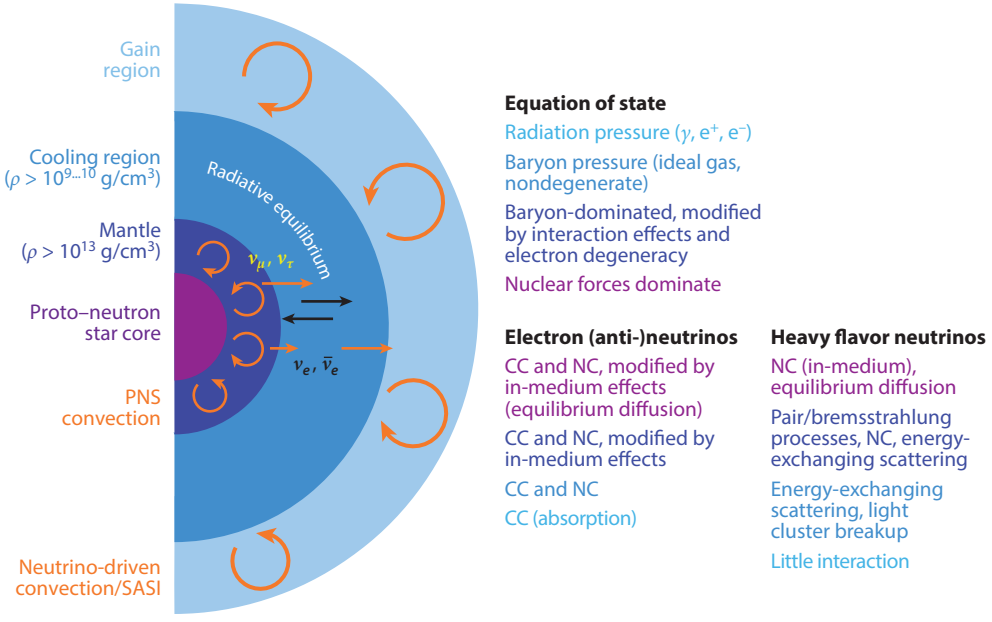

Figure 2

Sketch of the various regions in the supernova core, the equation-of-state and transport regimes, and the neutrino interaction processes that are most relevant for the dynamics and the observable neutrino signal (neglecting flavor oscillations). Abbreviations: CC, charged-current; NC, neutral-current; PNS, proto–neutron star; SASI, standing accretion-shock instability.

where the grayness factor ϕ accounts for the deviation from the Stefan–Boltzmann law. Equation 3 adequately describes the heavy-flavor luminosity, with the grayness parameter ϕ varying in the range from 0.4 to 0.6 during the pre-explosion and early explosion phases (78).

The emission of ν_e and $\bar{\nu}_e$ is fed not only by the diffusion of thermal energy from the PNS core but also by accretion energy. As the accreted matter settles onto the PNS surface, it enters into radiative equilibrium with deeper layers and must undergo net neutrino cooling to maintain a roughly constant temperature as it is compressed to higher densities. As ν_x can be produced only at high densities ($\gtrsim 10^{13}$ g cm^{-3}) by pair creation, nucleon bremsstrahlung (100), and neutrino pair conversion (50) and not by charged-current processes in the more dilute atmosphere,[1] cooling proceeds mostly by emission of ν_e and $\bar{\nu}_e$. Only about half of the accretion energy actually goes into ν_e and $\bar{\nu}_e$ (32, 78, 101), since the accreted matter does not cool below a radiative equilibrium temperature of several MeV.

Accounting for both the diffusive component and the accretion luminosity, the luminosities L_{ν_e} and $L_{\bar{\nu}_e}$ of ν_e and $\bar{\nu}_e$ are well described by (32, 101)

$$L_{\nu_e} + L_{\bar{\nu}_e} = 2\beta_1 L_{\nu_x} + \beta_2 \frac{GM\dot{M}}{R}, \qquad 4.$$

where M is the PNS mass, $\dot{M}$ is the mass accretion rate, and $\beta_1 = 1.25$ and $\beta_2 = 0.5$ (32, 101) are nondimensional parameters. The fact that $\beta_1 \neq 1$ reflects that the gray-body contribution need not be the same for ν_e, $\bar{\nu}_e$, and ν_x because the decoupling of ν_x from the matter works differently due to the absence of charged-current reactions at low densities.

[1] Charged-current production of ν_μ becomes relevant in the interior of the PNS due to the high temperatures and chemical potentials of electrons and ν_e (57).

Both ν_e and $\bar{\nu}_e$ carry roughly half of the electron-flavor luminosity. The exact split between ν_e and $\bar{\nu}_e$ is sensitive to the detailed neutrino interaction rates—for example, to the effect of nucleon potentials on the charged-current rates (54, 102), especially when the accretion rate drops during the explosion phase—and to the structure of the neutrinospheric region and the PNS convection zone below it (103).

During the accretion phase and the early explosion phase, the high-density EoS primarily influences the neutrino emission indirectly via the PNS radius and surface temperature given in Equations 3 and 4. EoSs that yield more compact PNSs result in higher neutrino luminosities and mean energies (6, 104). Over short timescales of hundreds of milliseconds, diffusion is too slow to transport significant amounts of energy and lepton number from the high-density core to the neutrinosphere, so the precise transport coefficients and thermodynamic properties well above saturation density have little direct effect on the neutrino signal. Even the heavy-flavor emission comes mostly from the extended mantle rather than from the core during the pre-explosion phase. This is not to say that nuclear interactions of the matter are unimportant for the neutrino emission during this phase, since they already affect the thermodynamic properties, composition, and transport coefficients well below nuclear saturation density, for instance, through correlation effects on the neutrino opacities (58, 105, 106). Many of the more recent corrections in the treatment of such in-medium effects typically affect the neutrino luminosities and mean energies on the level of a few percent (57, 58), which may be less relevant in the context of neutrino observations but can play an important role in shock revival (57).

Similar to the luminosities, the neutrino spectra carry information about the thermodynamic properties of the decoupling region. For ν_e and $\bar{\nu}_e$, the emerging spectra roughly reflect the energy-dependent equilibrium intensities at the neutrinosphere (107, 108). Because of the neutron-rich conditions at the PNS surface, the opacity for the absorption of $\bar{\nu}_e$ by protons is smaller than for the absorption of ν_e on neutrons, so that $\bar{\nu}_e$ decouple at smaller radii and higher temperatures. The mean energy of $\bar{\nu}_e$ is thus higher by approximately 2.5 MeV. The precise difference in mean energy is sensitive to the microphysics; in order to obtain accurate predictions, it is critical to include weak magnetism corrections (109), which increase the spread in mean energy by $\sim$0.5 MeV (25) as they decrease the opacity for $\bar{\nu}_e$, and (especially at later phases) the effects of nucleon interaction potentials on the charged-current rates (54, 102). The difference in mean energy remains remarkably constant with time in the most sophisticated simulation codes throughout the accretion phase (32, 78, 110, 111) and decreases only during the Kelvin–Helmholtz cooling phase over timescales of seconds.

Because the dominant opacities for ν_e and $\bar{\nu}_e$, namely absorption and scattering on nucleons, strongly depend on neutrino energy E_ν with the cross sections scaling roughly as $\sigma_0(E_\nu/m_e c^2)^2$ (where $\sigma_0 = 1.76 \times 10^{-44}\,\mathrm{cm}^2$), high-energy neutrinos decouple further outside and the emerging spectra are therefore "pinched" with a steeper high-energy tail compared with Fermi–Dirac spectra (107, 108, 112). The monochromatic neutrino number flux f_ν for pinched spectra can be conveniently parameterized by a generalized Maxwell–Boltzmann spectrum in terms of the mean energy $\langle E_\nu \rangle$ and a shape parameter α (112, 113),

$$f_\nu \propto E_\nu^\alpha e^{-(\alpha+1)E_\nu/\langle E_\nu \rangle}, \qquad 5.$$

which has no particular motivation other than the virtue of mathematical simplicity. Higher-energy moments $\langle E_\nu^n \rangle$,

$$\left\langle E_\nu^n \right\rangle = \frac{\int f_\nu E_\nu^n \, \mathrm{d}E_\nu}{\int f_\nu \, \mathrm{d}E_\nu}, \qquad 6.$$

Table 1 α parameters for high-resolution neutrino spectra from a $15M_\odot$ progenitor[a]

Species	Accretion phase (261 ms)	Early cooling phase (1,016 ms)	Intermediate cooling phase (1,991 ms)
ν_e	2.65	2.90	2.92
$\bar{\nu}_e$	3.13	2.78	2.61
ν_x	2.42	2.39	2.34

[a]All values are taken from the high-resolution case of Reference 113, table 1.

of the distribution function given by Equation 5 can be calculated recursively in terms of the shape parameter α as

$$\frac{\langle E_\nu^k \rangle}{\langle E_\nu^{k-1} \rangle} = \frac{k+\alpha}{1+\alpha} \langle E_\nu \rangle . \qquad 7.$$

Table 1 lists typical values of different stages based on the first and second energy moments from high-resolution spectra (113). Higher values of α indicate stronger pinching.

Spectrum formation is more complicated for ν_x: The emission and absorption of ν_x freeze out at higher densities and temperatures than for $\bar{\nu}_e$, but outside the so-called number sphere where the number flux of ν_μ, $\bar{\nu}_\mu$, ν_τ, and $\bar{\nu}_\tau$ is set, ν_x can still exchange energy with the medium via recoil in scattering reactions on nucleons (which is the dominant energy transfer mechanism during the accretion phase), electrons, and positrons out to an energy sphere. Since the average energy exchanged during neutrino–nucleon scattering is small, the energy sphere lies somewhat inside the surface of last scattering. The energy transfer can be sizable and reduce ν_x luminosities by $\lesssim$7% in this scattering layer (55). As a result, the expected hierarchy $\langle E_{\nu_e} \rangle < \langle E_{\bar{\nu}_e} \rangle < \langle E_{\nu_x} \rangle$ eventually changes to $\langle E_{\nu_e} \rangle < \langle E_{\nu_x} \rangle < \langle E_{\bar{\nu}_e} \rangle$. The crossover occurs earlier for higher accretion rates; in massive progenitors it may occur as early as ~200 ms after bounce. The ν_x spectrum remains less pinched than that of $\bar{\nu}_e$ with α parameters of $\alpha \approx 2.4$ (**Table 1**), however, so that one always has $\langle E_{\bar{\nu}_e}^2 \rangle < \langle E_{\nu_x}^2 \rangle$.

Interestingly, simulations and analytic considerations on the PNS surface structure suggest that $\langle E_{\bar{\nu}_e} \rangle$ is roughly proportional to the neutron star mass during the accretion phase. For the EoS presented in Reference 114 with a bulk incompressibility modulus of 220 MeV, one finds (78)

$$\langle E_{\bar{\nu}_e} \rangle \approx 10\,\mathrm{MeV}(M/M_\odot). \qquad 8.$$

However, the proportionality constant is not independent of the nuclear EoS, which can easily shift the mean energies by up to several MeV during the later accretion phase. Even for a given high-density EoS, there is a scatter of 15–20% around the correlation $\langle E_{\bar{\nu}_e} \rangle \propto M$ for different progenitors and epochs.

It has occasionally been suggested that ν_e and $\bar{\nu}_e$ also provide a diagnostic for the onset of the explosion via a sudden drop of the luminosity around shock revival because of the dependence on the mass accretion rate $\dot{M}$ (38). This, however, is only an artifact of one-dimensional (1D) explosion models in which the explosion is triggered by hand. Such a sudden drop is associated only with the infall of shell interfaces in the progenitor (see Section 4.2). In contrast to 1D explosion models, multidimensional models predict a slow decline of $\dot{M}$ after shock revival (78, 110, 111) because there is an extended phase of concurrent mass ejection and mass accretion. Although three-dimensional (3D) models show a faster decline of the accretion rate than two-dimensional (2D) models (79, 115), the decline is still drawn out over hundreds of milliseconds (**Figure 1*b***). It

is essentially impossible to distinguish whether such a gradual decline is due to shock revival or due to the progenitor structure.

4.2. Constraining Progenitor Properties

In principle, flavor-dependent neutrino luminosities and mean energies could be used to constrain the time dependence of the PNS mass M, radius R, and mass accretion rate $\dot{M}$ by use of Equations 3, 4, and 8. However, the amount of information that can actually be extracted in this way from a future Galactic event will strongly depend on the distance of the supernova from Earth, and both anisotropies in the neutrino emission (Section 4.3) and neutrino flavor conversion introduce uncertainties in the interpretation of the observed neutrino fluxes and spectra that cannot be easily factored out.

A prominent feature in the time-dependent neutrino flux that likely survives even with moderately high count rates is the drop in the ν_e and $\bar{\nu}_e$ luminosity that is associated with the drop in $\dot{M}$ after the accretion of the Si/O shell interface in many progenitor models (**Figure 1*a*,*b***). This drop is the consequence of a pronounced jump in entropy and density at an active shell source with vigorous O burning at the onset of collapse. The infall time for the Si/O interface varies from ∼100 ms in low-mass progenitors to several hundred milliseconds in high-mass progenitors. Merely by timing the infall of this shell interface, one can place important constraints on the progenitor structure, since the infall time t_{infall} of a shell is directly related to its mass coordinate m_{if} and precollapse radius r_{if}. Approximately, one finds (116, 117)

$$t_{\mathrm{infall}} \approx \sqrt{\frac{\pi^2 r_{\mathrm{if}}^3}{3Gm_{\mathrm{if}}}}, \qquad 9.$$

although numerical simulations should be used to match the measured arrival time of the shell interface in practice.

Even without recourse to the detailed time dependence of the neutrino signal, one can still obtain constraints on the progenitor core structure from integrated count rates. This was pointed out after SN 1987A (27, 29) and recently reinvestigated (104, 118) with the use of large sets of progenitor models. The authors of Reference 104 investigated the first 0.5 s of postbounce neutrino emission of progenitors between $12M_\odot$ and $120M_\odot$ in spherical symmetry (**Figure 3**). They showed that the energy emitted in $\bar{\nu}_e$ varies by approximately a factor of four across progenitors and is strongly correlated with the compactness ξ_m of the progenitor, which is essentially a normalized measure for the radius r of a specified mass shell m (119):

$$\xi_m = \frac{m/M_\odot}{r/1{,}000\,\mathrm{km}}. \qquad 10.$$

The progenitor variations in ν_x emission are less pronounced but still sizable. The compactness $\xi_{1.75}$ is a very good predictor of the total pre-explosion neutrino emission (104); even in the worst case of a full swap between $\bar{\nu}_e$ and $\bar{\nu}_x$, and even with a present-day detector (Super-K), the cumulative IBD event count from $\bar{\nu}_e$ is potentially a powerful diagnostic for the progenitor compactness. The same study (104) also addresses degeneracies and uncertainties that need to be overcome for a quantitative measurement of the compactness, such as a possible drop of the accretion rate after shock revival, flavor conversion, rotation, and uncertainties in the high-density EoS. Some of these degeneracies can be broken; specifically, uncertainties in the EoS can be eliminated by measuring both the time-integrated flux and the mean energy of the detected time-integrated spectrum from the pre-explosion phase (104).

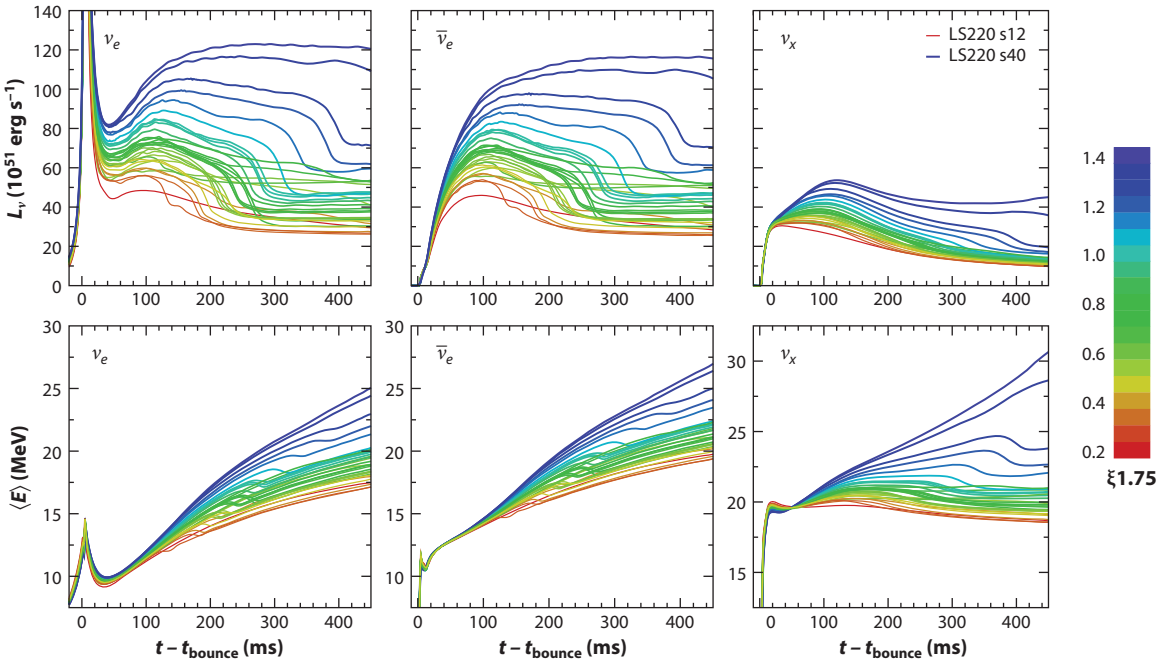

Figure 3

Neutrino luminosities L_ν and mean energies $\langle E \rangle$ for 32 progenitors with masses between $12M_\odot$ and $120M_\odot$ obtained with the LS220 equation of state (114). Colors indicate the progenitor compactness $\xi_{1.75}$; the trend toward higher luminosities and mean energies for increasing $\xi_{1.75}$ is evident. Figure adapted with permission from Reference 104; copyright 2013 The American Astronomical Society.

4.3. Imprint of Multidimensional Fluid Flow on the Neutrino Signal

Another obstacle for the interpretation of observed neutrino fluxes and spectra is that the neutrino emission will not be isotropic in the accretion phase and early explosion phase, which needs to be modeled using multidimensional neutrino transport (see the sidebar titled Challenges of Neutrino Transport in Three Dimensions). Electron-flavor neutrino emission is enhanced over accretion hot spots (122), and strong rotation can lead to hotter spectra and enhanced luminosities at high latitudes with somewhat different effects on electron flavor and ν_x (122, 123). Moreover, recent simulations have observed a strong global asymmetry in the lepton number flux (i.e., the difference between the number fluxes of ν_e and $\bar{\nu}_e$), which is connected to a slowly evolving, low-mode instability in the PNS convection zone (42, 48, 124–126). After independent corroboration with many neutrino transport codes, there is little doubt that this lepton number emission self-sustained asymmetry (LESA) (124) is not a numerical artifact, but the phenomenon is still not fully understood. There are some indications that it may be nothing more than a manifestation of buoyancy-driven PNS convection whose peculiarities—in particular, the slowly evolving dipole mode in the lepton number distribution—are related to the presence of partially stabilizing lepton number gradients and diffusive transport (42, 125, 126), but a rigorous theory of the LESA is still lacking.

Uncertainties from orientation effects are difficult to control for, but thankfully, they may be on a modest scale (except for the orientation effect on the lepton number flux) and dwarfed by uncertainties related to flavor conversion. In nonrotating 3D models, variations in the neutrino fluxes due to wandering accretion downflows remain below ∼10% and tend to average out over time. Systematic errors from latitudinal variations of the neutrino emission from rotating PNSs

CHALLENGES OF NEUTRINO TRANSPORT IN THREE DIMENSIONS

Capturing the effects of anisotropic neutrino emission on the dynamics and the observable neutrino signal requires multidimensional neutrino transport. Retaining the full six-dimensional phase-space dependence of the radiation field using discrete ordinate (135) or Monte Carlo methods (136) is still impractical for dynamical simulations over long timescales in three dimensions. Thus, various approximations for multidimensional transport are currently used:

- The ray-by-ray approximation (45, 51, 137) provides a straightforward way to generalize sophisticated transport algorithms for spherical symmetry to multiple dimensions by retaining only a parametric dependence of the radiation field on the angular coordinates in real space. It overestimates anisotropies in the neutrino emission, which can precipitate explosions in two dimensions (46, 138) but has little impact on the dynamics in three dimensions (139). Ray-by-ray simulations can be postprocessed to obtain more accurate fluxes and spectra for any given observer direction.
- Flux-limited diffusion without the ray-by-ray approximation artificially smears out anisotropies in the radiation field (123).
- Two-moment methods using an analytic closure have emerged (140–144) as a popular approximation that captures the anisotropies in the radiation field quite well.

As far as the observable signatures of anisotropic neutrino emission are concerned, there is no fundamental disagreement between postprocessed ray-by-ray models, Boltzmann transport, and two-moment transport.

are more difficult to eliminate, but constraints on the progenitor rotation from the gravitational wave signal may help (127).

Intriguingly, the modulation of the neutrino emission by asymmetric accretion onto the PNS can even be used to probe the dynamics of multidimensional flow in the supernova core. Simulations (123, 128) have already revealed that the prominent sloshing motions of the SASI in two dimensions are clearly mirrored in the neutrino signal for appropriate observer directions. Subsequent studies have established that these modulations are detectable by IceCube (78, 129–132), Hyper-K (132–134), DUNE, and JUNO (111). For SASI-dominated models, these accretion-induced modulations in the neutrino signal are every bit as strong in three dimensions as in two (132–134) and are visible to 10–20 kpc. Although they can be considerably less pronounced in models without SASI, they remain detectable with instruments such as IceCube, albeit only to a few kiloparsecs (130). Various studies have demonstrated that the frequency spectrum of the modulations shows clearly identifiable peaks that can be used to infer something of a typical, time-averaged SASI frequency (129, 132–134). Such peaks would not only serve as a smoking gun for SASI activity in the supernova core but would also quantitatively constrain the key parameters that determine its frequency, namely the shock radius and the radius of maximum deceleration (17), which is very similar to the PNS radius.

Given sufficiently violent fluid motions in the supernova core, the modulation of the neutrino signal can even be strong enough to deduce more detailed, time-dependent information on the dynamics from spectrograms of the signal (78, 132). This has been worked out most fully (78) for a range of exploding and nonexploding 2D models with the help of wavelet spectrograms of simulated signals in IceCube. **Figure 4** illustrates the diagnostic power of signal spectrograms using more recent 3D models, which were analyzed using the same assumptions as in Reference 78, that is, only MSW flavor conversion in the normal mass hierarchy and a simple detector model for IceCube. For SASI-dominated models of $18M_{\odot}$ (79) and $40M_{\odot}$ (121), the spectrogram shows

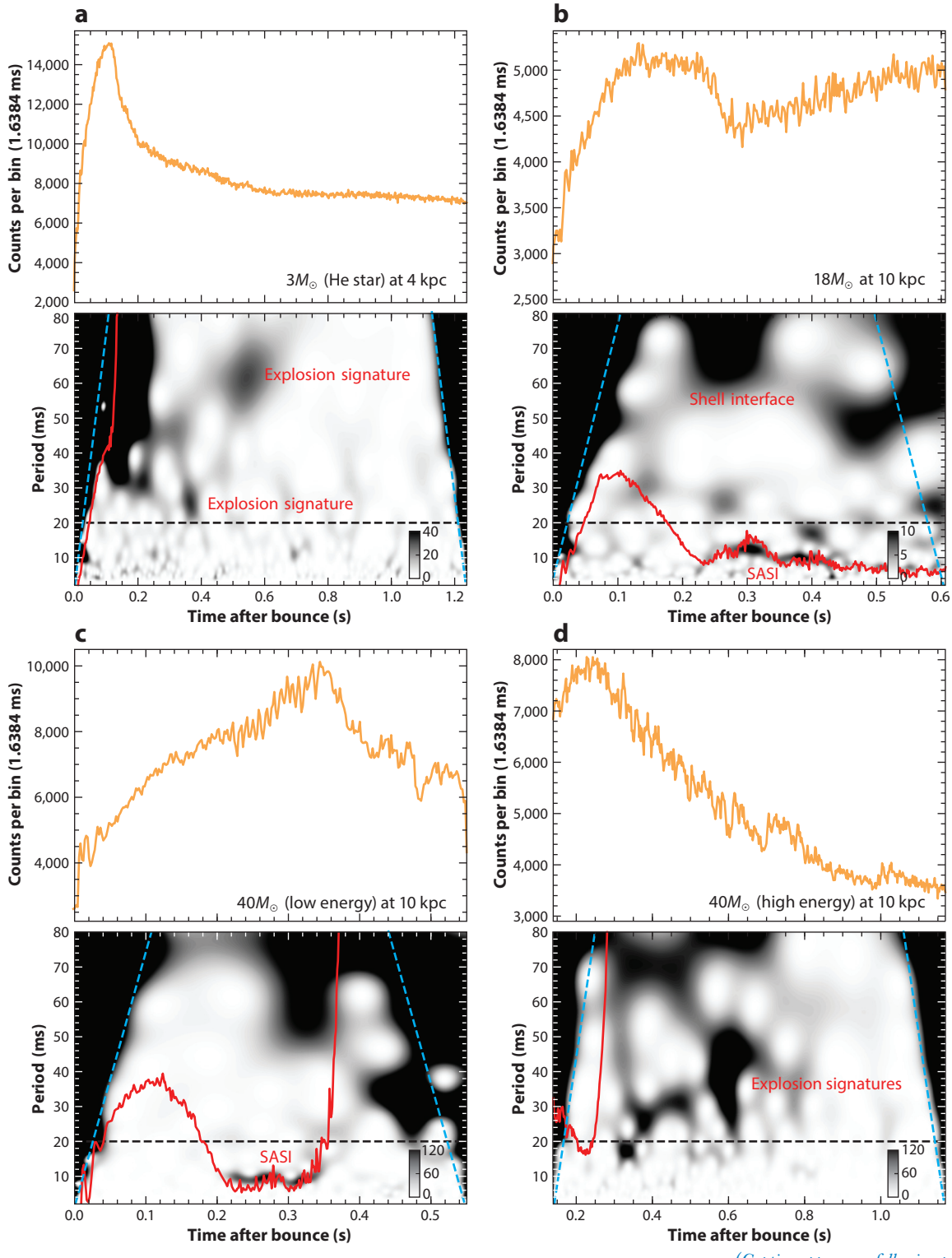

(*Caption appears on following page*)

Figure 4 (*Figure appears on preceding page*)

Simulated IceCube count rates (including noise) and their wavelet spectrograms for (*a*) a $3M_\odot$ He star (120) at 4 kpc, (*b*) the nonexploding $18M_\odot$ model (79), (*c*) the low-energy $40M_\odot$ model (121), and (*d*) a high-energy $40M_\odot$ case in which an explosion was triggered early by artificial preshock density perturbations (all at 10 kpc). The color in the spectrograms indicates the signal-to-noise ratio; dashed blue lines roughly demarcate the range of edge effects. The models illustrate the characteristic standing accretion-shock instability (SASI) fingerprint with its time-dependent frequency, which is well fitted by Equation 11 (*red curves*). Blobs at $\gtrsim$20 ms are a smoking gun for the development of an explosion, but they need to be carefully distinguished from edge effects and stripes from drops in the luminosity.

significant power at periods of ∼10 ms at late postbounce times. The time-dependent period $T_{\rm SASI}$ of the SASI peak is well described by

$$T_{\rm SASI} = 19\,{\rm ms}\left(\frac{r_{\rm sh,min}}{100\,{\rm km}}\right)^{3/2}\ln\left(\frac{r_{\rm sh,min}}{R}\right) \qquad 11.$$

in terms of the minimum shock radius $r_{\rm sh,min}$ and the PNS radius R (78). Combined with information on the PNS mass and radius from the neutrino luminosities and mean energies and, under favorable circumstances, gravitational waves (145), Equation 11 can in principle be used to constrain the shock trajectory.

The accretion-induced signal modulations also provide a telltale sign of the onset of the explosion, namely a shift of power beyond periods of ∼20 ms (78). Furthermore, the same study (78) found small bursts in the emission of ν_e and $\bar{\nu}_e$ due to episodic fallback in some models; similar phenomena can be observed in the 2D models presented in Reference 111. However, these signatures of the explosion are somewhat exaggerated by symmetry artifacts in 2D models, where the accretion downflows hit the PNS with higher velocities and the accretion rate fluctuates considerably more than in 3D models after shock revival (115). In three dimensions, the accretion-induced modulation of the neutrino signal tends to be much milder even when there is ongoing accretion after shock revival. In the case of the $3M_\odot$ He star model presented in Reference 120, the simulated spectrogram of the IceCube signal shows only the characteristic wavelet power at long periods for a supernova distance of 4 kpc (**Figure 4*a***). Strong explosion signatures survive only in massive progenitors with high accretion rates after shock revival, for example, in another, more energetic $40M_\odot$ model similar to that of Reference 121.

A recent study (132) considered the modulations of the neutrino emission as a probe of progenitor rotation. The authors found that rotation changes the amplitudes and the direction dependence of the signal modulation due to a number of effects that depend on the rotation rate and whose interplay appears to be quite intricate. They identified distinct features in the modulation spectra and spectrograms of rotating models, such as secondary peaks above the SASI frequency. Our understanding of these rotational effects is somewhat sketchy at present, however, and their diagnostic potential still needs to be investigated further.

4.4. Black Hole Formation and Phase-Transition Signatures

The time-dependent neutrino fluxes could provide further clues about the dynamics in the supernova core in the case of black hole formation, which would lead to a sharp cutoff of neutrino fluxes during the first seconds after bounce. Such a cutoff would likely be preceded only by a gradual rise of the neutrino luminosities and mean energies. Although some calculations (146) indicate that black hole formation could be associated with a noticeable rise in the heavy-flavor luminosities and several MeV in the mean energies of ν_μ and ν_τ as their neutrinosphere contracts strongly when the PNS approaches the critical mass for collapse, this strong rise disappears when the energy exchange with the medium in the scattering layer (see Section 4.1) is taken into account (32, 101).

The detection of such a cutoff could help resolve a number of questions in nuclear physics and astrophysics. In principle, the neutrino emission and the time of black hole formation are sensitive to the EoS (147), but they also depend on the progenitor (146), and it remains to be determined how well these factors can be disentangled by combining neutrino and electromagnetic observations. The astrophysical implications of a timed observation of black hole formation might be even broader. Simulations (121) and observational evidence from the composition of metal-poor stars (148) and of companions in high-mass X-ray binaries (HMXBs) (149), as well as from the kinematics of some HMXBs (149, 150), suggest that black hole formation can sometimes occur after shock revival due to fallback. A cutoff in the neutrino flux together with an explosion of sufficient energy would be direct proof of this scenario.

HMXB: high-mass X-ray binary

The neutrino signal may also reveal phase transitions at high densities in the PNS. More conservative scenarios of a late phase transition in the cooling are discussed in Section 5, but models for an early first-order phase transition at relatively low density have also been proposed. In this scenario, the phase transition leads to a second collapse of the PNS and the formation of a secondary shock that could trigger an explosion (24, 25). The formation of such a secondary shock would lead to a small, secondary neutrino burst. In contrast to the neutronization burst, this burst would be observed in all flavors and for both neutrinos and antineutrinos. $\bar{\nu}_e$ would be most abundantly emitted, however, because the hot β equilibrium is suddenly shifted to a higher Y_e by shock heating, so that the shocked matter protonizes. The signal of such a second burst in IceCube and Super-K has been analyzed (151): For the EoS in Reference 24, the brief increase of the detector count rates by a factor of several would serve as a clear fingerprint of the phase transition for a Galactic supernova even at a distance of 20 kpc. However, it remains to be determined whether such a secondary burst can be distinguished from temporal modulations of the neutrino signal by wandering accretion downflows and fallback, if the phase transition leads only to a weaker second bounce than in the models presented in References 24 and 25. Moreover, the viability of phase transition models is already limited by a number of other constraints. For example, the EoS originally used in Reference 24 is incompatible with the highest measured neutron star masses (152), and the light curves from powerful explosions driven by a phase-transition fall in the category of superluminous supernovae or peculiar SN 1987A–like type II-P supernovae (25), placing significant limits on the prevalence of this explosion scenario.

5. THE KELVIN–HELMHOLTZ COOLING PHASE

As accretion ceases, diffusive transport from within the PNS becomes the only source of neutrino emission in the Kelvin–Helmholtz cooling phase. As a result, the electron-flavor and heavy-flavor luminosities become relatively similar (**Figure 1*c***). The luminosities decrease roughly exponentially with a decay timescale of seconds. Despite the energy loss, the surface temperature and hence the mean energies of the neutrinos still increase for ∼1 s (32, 153) due to the contraction of the PNS.

The spectra of the different neutrino species remain different, with $\bar{\nu}_e$ maintaining higher mean energies than ν_e, so as to maintain a net lepton number flux out of the PNS. Modern simulations of the Kelvin–Helmholtz cooling phase show that the mean energies of ν_x remain below those of $\bar{\nu}_e$ due to recoil energy transfer in the scattering layer (153). As the PNS cools, the absolute differences in mean energy between the neutrino species shrink.

The demarcation between the accretion phase and the cooling phase is not a sharp one; rather, there is a gradual transition in the character of the neutrino emission. Although recent 3D explosion models show ongoing accretion at some level over timescales of seconds (79, 120), the neutrino emission in these 3D models already exhibits some features of the cooling phase a few

hundred milliseconds after shock revival, namely similar luminosities of all flavors and little short-term variation due to variable accretion downflows.

RPA: random phase approximation

5.1. Sensitivities of the Neutrino Emission

One of the key parameters determining the neutrino emission during the Kelvin–Helmholtz cooling phase is the neutron star binding energy $E_{\rm bind}$, which depends on the PNS mass and the EoS (see Equation 1). The major fraction of $E_{\rm bind}$ is radiated away after shock revival when the luminosities of all neutrino flavors have become similar. Thus, the total energy emitted in (anti)neutrinos of all three flavors is also similar (equipartition) and serves as a measure for $E_{\rm bind}$ that is not too strongly affected by uncertainties in flavor conversion. For example, the authors of Reference 153 have found good equipartition in their cooling models for an electron-capture supernova progenitor. For more massive progenitors with extended accretion, equipartition does not hold quite as well. Extrapolating the neutrino emission in the $18M_\odot$ explosion model presented in Reference 79 puts the total energy in each neutrino species to within 20% of the equipartition value $E_{\rm bind}/6$ (**Table 2**).

The time dependence of the neutrino luminosities and mean energies is sensitive to various factors. In contrast to the accretion phase, the stratification, thermodynamic conditions, and transport coefficients deep in the PNS now play a key role in shaping the neutrino emission as the slow evolution of the interior by neutrino diffusion makes itself felt in the neutrinospheric conditions. This makes the cooling phase a better laboratory for uncertain nuclear physics well above saturation density. However, it is not trivial to extricate the underlying physics from the neutrino fluxes and spectra, since different effects and nuclear physics parameters can affect the neutrino emission in a similar way.

Among the most important factors regulating the duration of the cooling phase are the neutrino opacities around and above saturation density. In the relevant equilibrium diffusion regime, it is the total Rosseland-averaged opacity that determines the energy and lepton number flux; thus, the most critical opacities are those for charged-current absorption and neutral-current scattering. At high densities, these are strongly affected by in-medium (correlation) effects (58, 105, 106, 154).

That in-medium effects can significantly change the PNS cooling timescale was realized decades ago (e.g., 155, 156). The first modern cooling models (32, 101, 153) including nucleon correlations following the random phase approximation (RPA) framework presented in References 105 and 106 predicted considerably shorter cooling times of the order of seconds due to the reduced opacities at high densities, rather than tens of seconds in older models (156–158). However, whereas measurements can be used to constrain correlation effects at moderate densities using the virial approach (58), considerable uncertainties remain in the relevant high-density opacities well

Table 2 Energy budget for the different neutrino species in an $18M_\odot$ star

Species	Energy up to $t = 2.4$ s[a] (10^{52} erg)	Residual energy[b] (10^{52} erg)	Total (10^{52} erg)	Relative to equipartition
ν_e	5.2	3.3	8.5	+20%
$\bar{\nu}_e$	4.8	3.3	8.1	+16%
ν_x	3.1	3.3	6.4	−9%
Total	22.4	19.6	42	NA

[a]Obtained by numerical integration of the luminosities from Reference 79.
[b]Obtained assuming equipartition after 2.4 s after bounce and a binding energy of 4.2×10^{53} erg for a putative neutron star mass of $1.67M_\odot$.
Abbreviation: NA, not applicable.

above saturation density. Moreover, many-body effects do not invariably lead to a reduction of the opacities, which can also have a noticeable effect on the neutrino emission from the cooling phase even though enhanced opacities may only apply in a thin layer near the PNS surface. For example, the authors of Reference 159 considered the effect of an enhanced neutral-current scattering opacity due to the formation of nuclear pasta and found a delay of the cooling with significantly increased neutrino luminosities and mean energies at late times.

The high-density EoS also affects the emission from the cooling phase in other ways. Differences in neutron star radius and the location of β equilibrium translate into differences in the gradients of the temperature and neutrino chemical potential that drive the diffusive energy and lepton number flux, and also affect the Rosseland-averaged neutrino opacities as these depend on density, temperature, and lepton number. In addition, the EoS affects the extent of the convective region inside the PNS during the cooling phase (32, 160). The resulting EoS dependence of the cooling and deleptonization timescale is nontrivial, and while there appears to be a weak trend toward shorter cooling timescales for stiffer EoSs (32, 101), no hard-and-fast rule can be given. Moreover, the cooling timescale also depends on the PNS mass M, with a trend toward a longer cooling time for higher M (101).

One signal feature whose connection to the underlying EoS physics has been explained in some detail is a break in the neutrino luminosity that occurs in models in which the convection zone disappears during the cooling phase (**Figure 5**) (160). The disappearance of the convection zone,

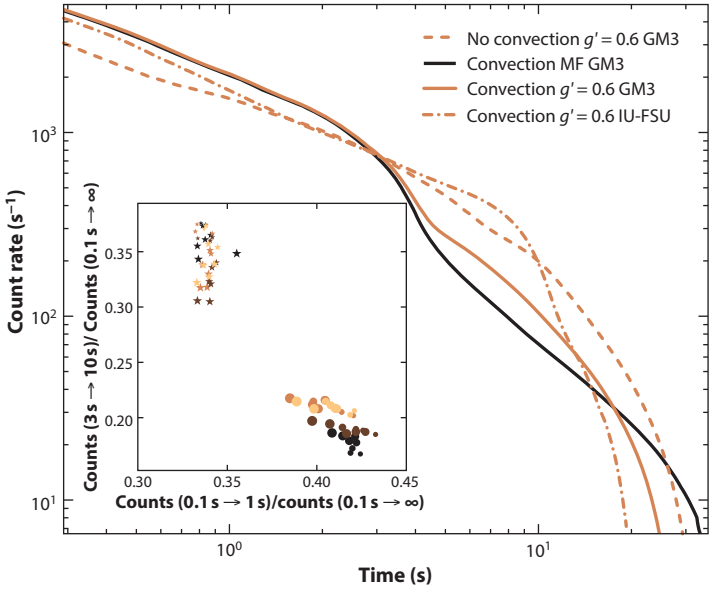

Figure 5

Count rates in Super-Kamiokande for proto–neutron star (PNS) cooling models with $M = 1.6M_\odot$, with and without mixing-length convection for different equations of state (EoSs) (GM3 versus IU-FSU), and different values of the Migdal parameter ($g' = 0.3$ versus $g' = 0.6$) in the calculation of random phase approximation (RPA) opacities. One model (*black curve*) has been calculated using opacities based on the mean-field (MF) approximation instead of the RPA. The break of the luminosities in the convective models indicates the disappearance of the PNS convection zone, which occurs at different times for the two EoSs. (*Inset*) The fraction of counts after 3 s and before 1 s can be used to separate the two EoSs (*circles*, GM3; *stars*, IU-FSU) for a number of cooling models with PNS masses between $1.2M_\odot$ and $2.1M_\odot$. Figure adapted with permission from Reference 160; copyright 2012 American Physical Society.

and hence the break in the neutrino light curves, can be related to the derivative $\partial E_{\rm sym}/\partial\rho$ of the nuclear symmetry energy $E_{\rm sym}$; large values of $\partial E_{\rm sym}/\partial\rho$ favor the earlier termination of convection because they imply a stronger stabilizing effect of the negative lepton number gradients under the conditions encountered during the cooling phase (i.e., low temperatures and Y_e close to β equilibrium).

It is also possible that some phase transition occurs during the PNS cooling case. Unlike the phase-transition scenario described in Section 4.4, such a phase transition would not be triggered by additional accretion but merely by the contraction of the PNS during the cooling phase and the ongoing deleptonization. Studies that investigated the appearance of hyperons or a phase transition to a kaon condensate or quark matter during the cooling phase determined that the cleanest signature for such a phenomenon would be a cutoff of the neutrino flux in case the phase transition triggers collapse to a black hole at late times; otherwise, the effect on the neutrino light curves is small (157, 161, 162). However, the scenario of delayed collapse needs to be revisited with updated EoS models in light of more recent constraints on the high-density EoS, such as better limits on the maximum neutron star mass (163) and on neutron star radii (e.g., 164).

5.2. Constraints on Exotic Energy Loss Channels

It has long been known that the time-integrated neutrino flux and the duration of the neutrino signal can be used to place constraints on the emission of hypothetical particles such as axions, sterile right-handed neutrinos (165), and Kaluza–Klein gravitons (166) that would carry away a sizable fraction of the PNS binding energy. In particular, cooling by axions has been studied extensively. The detection of neutrinos from SN 1987A has already helped to place an upper limit on the axion mass m_a; since then, initial estimates of an upper limit of $m_a \lesssim 10^{-3}$ eV (167–169) have been weakened to $m_a \lesssim 10^{-2}$ eV (with the precise limit depending somewhat on the axion model) because of many-body effects that modify the axion cooling rate (170, 171). Prospects for better bounds on the axion mass from a Galactic supernova have recently been investigated (172), but the results do not promise substantially better bounds ($m_a \lesssim 10^{-2}$ eV) from the neutrino light curves.

For some of these exotic particles, there does not appear to be much room for improved bounds due to better detection statistics, since this would require tracking down extra energy loss that amounts to only a small fraction of the neutron star binding energy. At this level, uncertainties in the neutron star mass, radius, and EoS can no longer be ignored.

In some scenarios, specifically those involving sterile neutrinos (e.g., 173) or nonstandard neutrino interactions (e.g., 174), one would expect clearer signatures in the neutrino emission (not necessarily during the cooling phase) from a nearby supernova with sufficiently high neutrino count rates and sufficient temporal resolution. For example, there is the possibility of energy-dependent jumps in the observed neutrino fluxes as the conditions for flavor conversion, and hence the survival probabilities of observable flavors, change (173).

5.3. Shock Propagation Effects

Beyond serving as a probe of the conditions in the PNS, the signal from the cooling phase may also provide clues about the explosion dynamics. For normal Fe-core progenitors with shallow density profiles, the shock traverses the MSW resonance regions during the cooling phase, and as a result MSW flavor conversion becomes nonadiabatic (175–177). Such a change in MSW flavor conversion could lead to detectable changes in the neutrino spectra or other convenient measures that are sensitive to flavor conversion, such as the ratio of charged-current to neutral-current event rates (178). Similarly, MSW flavor conversion will be affected by the formation and

propagation of a reverse shock in the wake of shock deceleration (177). This prospect of such a late-time signature from shock propagation in the neutrinos signal is intriguing, but there are several complications. Since multidimensional fluid instabilities already play a major role during the phase of shock revival and also later on as the shocked shells become unstable to Rayleigh–Taylor mixing, the phenomenology of MSW flavor conversion is affected by stochastic fluctuations of the density (and hence of the matter potential) behind the shock. These can modulate and even suppress oscillation signatures (179–181). Our incomplete understanding of collective flavor conversion also presents a problem. Finally, since much of the research on the signatures of shock propagation and turbulence still assumes larger spectral differences between flavors than have been obtained in modern simulations of the cooling phase, many findings on the associated neutrino signatures deserve to be revisited at some point.

SUMMARY POINTS

1. Detailed time-dependent information on the neutrino fluxes and spectra, expected from current and future neutrino detectors with complementary designs, is the key to exploiting neutrinos as a diagnostic of core-collapse supernovae.
2. The ν_e burst and the early postbounce phase can provide a handle on the supernova distance, the neutrino mass ordering, and possibly the progenitor structure in the case of an electron-capture supernova. The rise of the signal also provides precise timing information, which is relevant for gravitational wave detection.
3. During the accretion phase, flavor-dependent fluxes and spectra would help place constraints on the time-dependent PNS surface temperature, mass, and radius and the accretion rate via the Stefan–Boltzmann law, the excess accretion luminosity of ν_e and $\bar{\nu}_e$, and the relation $\langle E_{\bar{\nu}_e} \rangle \propto M$.
4. Barring uncertainties concerning flavor transformation, the time-integrated neutrino emission during the accretion phase can be used to infer the progenitor compactness, and the position of the Si/O shell interface can be constrained using the characteristic drop in electron-flavor luminosity.
5. The modulation of the neutrino emission by the time-varying accretion flow onto the PNS can be used to infer the presence of the SASI and measure the time dependence of the SASI frequency, which is related to the shock radius. Temporal modulations with periods $\gtrsim$20 ms serve as an indicator of a developing explosion.
6. The neutrino emission from the Kelvin–Helmholtz cooling phase serves as a probe of the structure and microphysics (high-density EoS, opacities) of the PNS interior. The time-integrated flux constrains the neutron star binding energy and is relatively robust against uncertainties from flavor conversion because of approximate flavor equipartition in the cooling phase.

FUTURE ISSUES

1. Although supernova simulations have matured considerably, there will still be room in the coming decade for further technical improvements, a better exploration of

parameter space (ideally by means of 3D simulations from collapse into the cooling phase), and broader replication of results by different groups in order to understand the phenomenology of supernova neutrino emission.

2. Flavor conversion remains a thorny issue for inferring supernova physics from the neutrino signal. If it turns out that fast flavor conversion can occur in the neutrinospheric region during the accretion phase, this would pose a serious challenge for supernova modeling and force us to revise many of the current neutrino signal predictions.
3. Although this review has focused on the once-in-a-lifetime chance of a Galactic supernova, there is also the possibility of exploiting the diffuse supernova neutrino background (see References 32, 182, and 183 for extensive reviews). The diffuse supernova neutrino background will provide complementary information, in particular, on the fraction of failed supernovae (184) and hence on the mass range for successful explosions (33).

DISCLOSURE STATEMENT

The author is not aware of any affiliations, memberships, funding, or financial holdings that might be perceived as affecting the objectivity of this review.

ACKNOWLEDGMENTS

I thank E. O'Connor and L. Roberts for permission to use **Figures 3** and **5**, respectively. The writing of this review was supported by the Australian Research Council (ARC) through ARC Future Fellowship FT160100035. This research was undertaken with the assistance of resources obtained via the National Computational Merit Allocation Scheme and Astronomy Supercomputer Time Allocation Committee from the National Computational Infrastructure, which is supported by the Australian Government and was supported by resources provided by the Pawsey Supercomputing Centre with funding from the Australian Government and the Government of Western Australia.

LITERATURE CITED

1. Hirata K, et al. *Phys. Rev. Lett.* 58:1490 (1987)
2. Bionta RM, et al. *Phys. Rev. Lett.* 58:1494 (1987)
3. Alexeyev EN, Alexeyeva LN, Krivosheina IV, Volchenko VI. *Phys. Lett. B* 205:209 (1988)
4. Bruenn SW. *Astrophys. J. Suppl.* 58:771 (1985)
5. Bethe HA. *Rev. Mod. Phys.* 62:801 (1990)
6. Janka H-T, et al. *Phys. Rep.* 442:38 (2007)
7. Mezzacappa A. *Annu. Rev. Nucl. Part. Sci.* 55:467 (2005)
8. Janka H-T. *Annu. Rev. Nucl. Part. Sci.* 62:407 (2012)
9. Burrows A. *Rev. Mod. Phys.* 85:245 (2013)
10. Müller B. *Publ. Astron. Soc. Aust.* 33:e048 (2016)
11. Bethe HA, Wilson JR. *Astrophys. J.* 295:14 (1985)
12. Kitaura FS, Janka H-T, Hillebrandt W. *Astron. Astrophys.* 450:345 (2006)
13. Herant M, et al. *Astrophys. J.* 435:339 (1994)
14. Burrows A, Hayes J, Fryxell BA. *Astrophys. J.* 450:830 (1995)
15. Janka H-T, Müller E. *Astron. Astrophys.* 306:167 (1996)
16. Blondin JM, Mezzacappa A, DeMarino C. *Astrophys. J.* 584:971 (2003)

17. Foglizzo T, Galletti P, Scheck L, Janka H-T. *Astrophys. J.* 654:1006 (2007)
18. Akiyama S, et al. *Astrophys. J.* 584:954 (2003)
19. Burrows A, et al. *Astrophys. J.* 664:416 (2007)
20. Winteler C, et al. *Astrophys. J.* 750:L22 (2012)
21. Mösta P, et al. *Astrophys. J.* 785:L29 (2014)
22. Faucher-Giguère CA, Kaspi VM. *Astrophys. J.* 643:332 (2006)
23. Mosser B, et al. *Astron. Astrophys.* 548:A10 (2012)
24. Sagert I, et al. *Phys. Rev. Lett.* 102:081101 (2009)
25. Fischer T, et al. *Nat. Astron.* 2:980 (2018)
26. Lattimer JM, Prakash M. *Astrophys. J.* 550:426 (2001)
27. Bruenn SW. *Phys. Rev. Lett.* 59:938 (1987)
28. Bahcall JN, Piran T, Press WH, Spergel DN. *Nature* 327:682 (1987)
29. Burrows A. *Astrophys. J.* 334:891 (1988)
30. Arnett WD, Bahcall JN, Kirshner RP, Woosley SE. *Annu. Rev. Astron. Astrophys.* 27:629 (1989)
31. Janka H-T. In *Handbook of Supernovae*, ed. AW Alsabti, P Murdin, p. 1575. Berlin: Springer (2017)
32. Mirizzi A, et al. *Nuovo Cim. Riv. Ser.* 39:1 (2016)
33. Horiuchi S, Kneller JP. *J. Phys. G* 45:043002 (2018)
34. Ikeda M, et al. *Astrophys. J.* 669:519 (2007)
35. Hyper-Kamiokande Work. Group. arXiv:1309.0184 [hep-ex] (2013)
36. Abbasi R, et al. *Astron. Astrophys.* 535:A109 (2011)
37. An F, et al. *J. Phys. G* 43:030401 (2016)
38. Wurm M, et al. *Astropart. Phys.* 35:685 (2012)
39. Vasel JA, Sheshukov A, Habig A. arXiv:1710.00705 [astro-ph] (2017)
40. Acciarri R, et al. arXiv:1601.05471 [hep-ex] (2016)
41. Scholberg K. *Annu. Rev. Nucl. Part. Sci.* 62:12072 (2012)
42. Janka H-T, Melson T, Summa A. *Annu. Rev. Nucl. Part. Sci.* 66:341 (2016)
43. Messer OEB, Mezzacappa A, Bruenn SW, Guidry MW. *Astrophys. J.* 507:353 (1998)
44. Liebendörfer M, Rampp M, Janka H-T, Mezzacappa A. *Astrophys. J.* 620:840 (2005)
45. Müller B, Janka H-T, Dimmelmeier H. *Astrophys. J. Suppl.* 189:104 (2010)
46. Just O, et al. *Mon. Not. R. Astron. Soc.* 481:4786 (2018)
47. Kotake K, et al. *Astrophys. J.* 853:170 (2018)
48. O'Connor E, et al. *J. Phys. G* 45:104001 (2018)
49. Pan KC, et al. *J. Phys. G* 46:014001 (2019)
50. Buras R, et al. *Astrophys. J.* 587:320 (2003)
51. Buras R, Rampp M, Janka H-T, Kifonidis K. *Astron. Astrophys.* 447:1049 (2006)
52. Lentz EJ, et al. *Astrophys. J.* 747:73 (2012)
53. Lentz EJ, et al. *Astrophys. J.* 760:94 (2012)
54. Martínez-Pinedo G, Fischer T, Lohs A, Huther L. *Phys. Rev. Lett.* 109:251104 (2012)
55. Müller B, Janka H-T, Marek A. *Astrophys. J.* 756:84 (2012)
56. Bartl A, Bollig R, Janka H-T, Schwenk A. *Phys. Rev. D* 94:083009 (2016)
57. Bollig R, et al. *Phys. Rev. Lett.* 119:242702 (2017)
58. Horowitz CJ, et al. *Phys. Rev. C* 95:025801 (2017)
59. Duan H, Fuller GM, Qian YZ. *Annu. Rev. Nucl. Part. Sci.* 60:569 (2010)
60. Wolfenstein L. *Phys. Rev. D* 17:2369 (1978)
61. Mikheyev SP, Smirnov AY. *Yad. Fiz.* 42:1441 (1985)
62. Pantaleone J. *Phys. Lett. B* 287:128 (1992)
63. Pastor S, Raffelt GG. *Phys. Rev. Lett.* 89:191101 (2002)
64. Sawyer RF. *Phys. Rev. D* 79:105003 (2009)
65. Raffelt GG, Sarikas S, de Sousa Seixas D. *Phys. Rev. Lett.* 111:091101 (2013)
66. Mirizzi A. *Phys. Rev. D* 88:073004 (2013)
67. Mirizzi A, Mangano G, Saviano N. *Phys. Rev. D* 92:021702 (2015)
68. Dasgupta B, Mirizzi A. *Phys. Rev. D* 92:125030 (2015)

69. Sarikas S, de Sousa Seixas D, Raffelt GG. *Phys. Rev. D* 86:125020 (2012)
70. Morinaga T, Yamada S. *Phys. Rev. D* 97:023024 (2018)
71. Chakraborty S, et al. *Phys. Rev. Lett.* 107:151101 (2011)
72. Sarikas S, Raffelt GG, Hüdepohl L, Janka H-T. *Phys. Rev. Lett.* 108:061101 (2012)
73. Odrzywolek A, Misiaszek M, Kutschera M. *Astropart. Phys.* 21:303 (2004)
74. Kato C, et al. *Astrophys. J.* 808:168 (2015)
75. Yoshida T, Takahashi K, Umeda H, Ishidoshiro K. *Phys. Rev. D* 93:123012 (2016)
76. Asakura K, et al. *Astrophys. J.* 818:91 (2016)
77. Patton KM, Lunardini C, Farmer RJ. *Astrophys. J.* 840:2 (2017)
78. Müller B, Janka H-T. *Astrophys. J.* 788:82 (2014)
79. Müller B, Melson T, Heger A, Janka H-T. *Mon. Not. R. Astron. Soc.* 472:491 (2017)
80. Kachelrieß M, et al. *Phys. Rev. D* 71:063003 (2005)
81. Serpico PD, et al. *Phys. Rev. D* 85:085031 (2012)
82. Nomoto K. *Astrophys. J.* 277:791 (1984)
83. Nomoto K. *Astrophys. J.* 322:206 (1987)
84. Jones S, et al. *Astrophys. J.* 772:150 (2013)
85. Duan H, Fuller GM, Carlson J, Qian YZ. *Phys. Rev. Lett.* 100:021101 (2008)
86. Lunardini C, Müller B, Janka H-T. *Phys. Rev. D* 78:023016 (2008)
87. Jones S, et al. *Astron. Astrophys.* 593:A72 (2016)
88. Doherty CL, Gil-Pons P, Siess L, Lattanzio JC. *Publ. Astron. Soc. Aust.* 34:e056 (2017)
89. Nomoto K, Leung SC. In *Handbook of Supernovae*, ed. AW Alsabti, P Murdin, p. 483. Berlin: Springer (2017)
90. Poelarends AJT, Herwig F, Langer N, Heger A. *Astrophys. J.* 675:614 (2008)
91. Nomoto K, et al. *Nature* 299:803 (1982)
92. Smith N. *Mon. Not. R. Astron. Soc.* 434:102 (2013)
93. Botticella MT, et al. *Mon. Not. R. Astron. Soc.* 398:1041 (2009)
94. Pastorello A, et al. *Mon. Not. R. Astron. Soc.* 394:2266 (2009)
95. Halzen F, Raffelt GG. *Phys. Rev. D* 80:087301 (2009)
96. Yokozawa T, et al. *Astrophys. J.* 811:86 (2015)
97. Dimmelmeier H, Ott CD, Marek A, Janka H-T. *Phys. Rev. D* 78:064056 (2008)
98. Ott CD, et al. *Phys. Rev. D* 86:024026 (2012)
99. Langanke K, et al. *Phys. Rev. Lett.* 90:241102 (2003)
100. Hannestad S, Raffelt GG. *Astrophys. J.* 507:339 (1998)
101. Hüdepohl L. 2014. *Neutrinos from the formation, cooling, and black hole collapse of neutron stars*. PhD thesis, Tech. Univ. München, Ger.
102. Roberts LF, Reddy S, Shen G. *Phys. Rev. C* 86:065803 (2012)
103. Buras R, Janka H-T, Rampp M, Kifonidis K. *Astron. Astrophys.* 457:281 (2006)
104. O'Connor E, Ott CD. *Astrophys. J.* 762:126 (2013)
105. Burrows A, Sawyer RF. *Phys. Rev. C* 58:554 (1998)
106. Burrows A, Sawyer RF. *Phys. Rev. C* 59:510 (1999)
107. Janka H-T, Hillebrandt W. *Astron. Astrophys. Suppl.* 78:375 (1989)
108. Janka H-T, Hillebrandt W. *Astron. Astrophys.* 224:49 (1989)
109. Horowitz CJ. *Phys. Rev. D* 65:043001 (2002)
110. Bruenn SW, et al. *Astrophys. J.* 818:123 (2016)
111. Seadrow S, et al. *Mon. Not. R. Astron. Soc.* 480:4710 (2018)
112. Keil MT, Raffelt GG, Janka H-T. *Astrophys. J.* 590:971 (2003)
113. Tamborra I, et al. *Phys. Rev. D* 86:125031 (2012)
114. Lattimer JM, Swesty FD. *Nucl. Phys. A* 535:331 (1991)
115. Müller B. *Mon. Not. R. Astron. Soc.* 453:287 (2015)
116. Woosley SE, Heger A. *Astrophys. J.* 806:145 (2015)
117. Müller B, Heger A, Liptai D, Cameron JB. *Mon. Not. R. Astron. Soc.* 460:742 (2016)
118. Horiuchi S, Nakamura K, Takiwaki T, Kotake K. *J. Phys. G* 44:114001 (2017)

119. O'Connor E, Ott CD. *Class. Quantum Gravity* 27:114103 (2010)
120. Müller B, et al. *Mon. Not. R. Astron. Soc.* 484:3307 (2019)
121. Chan C, et al. *Astrophys. J.* 852:L19 (2018)
122. Marek A, Janka H-T. *Astrophys. J.* 694:664 (2009)
123. Ott CD, Burrows A, Dessart L, Livne E. *Astrophys. J.* 685:1069 (2008)
124. Tamborra I, et al. *Astrophys. J.* 792:96 (2014)
125. Glas R, et al. arXiv:1809.10150 [astro-ph] (2018)
126. Powell J, Müller B. arXiv:1812.05738 (2018)
127. Abdikamalov E, Gossan S, DeMaio AM, Ott CD. *Phys. Rev. D* 90:044001 (2014)
128. Marek A, Janka H-T, Müller E. *Astron. Astrophys.* 496:475 (2009)
129. Lund T, et al. *Phys. Rev. D* 82:063007 (2010)
130. Lund T, et al. *Phys. Rev. D* 86:105031 (2012)
131. Brandt TD, Burrows A, Ott CD, Livne E. *Astrophys. J.* 728:8 (2011)
132. Walk L, Tamborra I, Janka H-T, Summa A. *Phys. Rev. D* 98:123001 (2018)
133. Tamborra I, et al. *Phys. Rev. Lett.* 111:121104 (2013)
134. Tamborra I, et al. *Phys. Rev. D* 90:045032 (2014)
135. Nagakura H, et al. *Astrophys. J. Suppl.* 229:42 (2017)
136. Abdikamalov E, et al. *Astrophys. J.* 755:111 (2012)
137. Bruenn SW, et al. arXiv:1809.05608 [astro-ph] (2018)
138. Skinner MA, Burrows A, Dolence JC. *Astrophys. J.* 831:81 (2016)
139. Glas R, Just O, Janka H-T, Obergaulinger M. *Astrophys. J.* 873:45 (2019)
140. Just O, Obergaulinger M, Janka H-T. *Mon. Not. R. Astron. Soc.* 453:3386 (2015)
141. Roberts LF, et al. *Astrophys. J.* 831:98 (2016)
142. Kuroda T, Takiwaki T, Kotake K. *Astrophys. J. Suppl.* 222:20 (2016)
143. Skinner MA, et al. *Astrophys. J. Suppl.* 241:7 (2019)
144. O'Connor EP, Couch SM. *Astrophys. J.* 854:63 (2018)
145. Müller B, Janka H-T, Marek A. *Astrophys. J.* 766:43 (2013)
146. Fischer T, et al. *Astron. Astrophys.* 499:1 (2009)
147. Sumiyoshi K, Yamada S, Suzuki H. *Astrophys. J.* 667:382 (2007)
148. Keller SC, et al. *Nature* 506:463 (2014)
149. Podsiadlowski P, et al. *Astrophys. J.* 567:491 (2002)
150. Repetto S, Davies MB, Sigurdsson S. *Mon. Not. R. Astron. Soc.* 425:2799 (2012)
151. Dasgupta B, et al. *Phys. Rev. D* 81:103005 (2010)
152. Antoniadis J, et al. arXiv:1605.01665 [astro-ph] (2016)
153. Hüdepohl L, et al. *Phys. Rev. Lett.* 104:251101 (2010)
154. Reddy S, Prakash M, Lattimer JM, Pons JA. *Phys. Rev. C* 59:2888 (1999)
155. Sawyer RF. *Phys. Rev. Lett.* 75:2260 (1995)
156. Keil W, Janka H-T, Raffelt GG. *Phys. Rev. D* 51:6635 (1995)
157. Pons JA, et al. *Astrophys. J.* 513:780 (1999)
158. Fischer T, et al. *Astron. Astrophys.* 517:A80 (2010)
159. Horowitz CJ, et al. arXiv:1611.10226 [astro-ph] (2016)
160. Roberts LF, et al. *Phys. Rev. Lett.* 108:061103 (2012)
161. Pons JA, Miralles JA, Prakash M, Lattimer JM. *Astrophys. J.* 553:382 (2001)
162. Pons JA, Steiner AW, Prakash M, Lattimer JM. *Phys. Rev. Lett.* 86:5223 (2001)
163. Antoniadis J, et al. *Science* 340:448 (2013)
164. Bauswein A, Just O, Janka H-T, Stergioulas N. *Astrophys. J.* 850:L34 (2017)
165. Raffelt GG, Seckel D, Sigl G. *Phys. Rev. D* 54:2784 (1996)
166. Hannestad S, Raffelt GG. *Phys. Rev. Lett.* 87:051301 (2001)
167. Turner MS. *Phys. Rev. Lett.* 60:1797 (1988)
168. Raffelt GG, Seckel D. *Phys. Rev. Lett.* 60:1793 (1988)
169. Mayle R, et al. *Phys. Lett. B* 203:188 (1988)
170. Janka H-T, Keil W, Raffelt GG, Seckel D. *Phys. Rev. Lett.* 76:2621 (1996)

171. Keil W, et al. *Phys. Rev. D* 56:2419 (1997)
172. Fischer T, et al. *Phys. Rev. D* 94:085012 (2016)
173. Esmaili A, Peres OLG, Serpico PD. *Phys. Rev. D* 90:033013 (2014)
174. Esteban-Pretel A, Tomàs R, Valle JWF. *Phys. Rev. D* 76:053001 (2007)
175. Schirato RC, Fuller GM. arXiv:astro-ph/0205390 (2002)
176. Fogli GL, Lisi E, Mirizzi A, Montanino D. *Phys. Rev. D* 68:033005 (2003)
177. Tomàs R, et al. *J. Cosmol. Astropart. Phys.* 9:015 (2004)
178. Kneller JP, McLaughlin GC, Brockman J. *Phys. Rev. D* 77:045023 (2008)
179. Friedland A, Gruzinov A. arXiv:astro-ph/0607244 (2006)
180. Fogli G, Lisi E, Mirizzi A, Montanino D. *J. Cosmol. Astropart. Phys.* 6:012 (2006)
181. Kneller J, Volpe C. *Phys. Rev. D* 82:123004 (2010)
182. Beacom JF. *Annu. Rev. Nucl. Part. Sci.* 60:439 (2010)
183. Lunardini C. *Astropart. Phys.* 79:49 (2016)
184. Lunardini C. *Phys. Rev. Lett.* 102:231101 (2009)